

Structures of *Mycobacterium tuberculosis* 1-Deoxy-D-xylulose-5-phosphate Reductoisomerase Provide New Insights into Catalysis*

Received for publication, March 6, 2007, and in revised form, April 5, 2007 Published, JBC Papers in Press, May 9, 2007, DOI 10.1074/jbc.M701935200

Lena M. Henriksson[‡], Torsten Unge[‡], Jens Carlsson[‡], Johan Åqvist[‡], Sherry L. Mowbray[§], and T. Alwyn Jones^{‡1}

From the [‡]Department of Cell and Molecular Biology, Uppsala University, Biomedical Center, Box 596, SE-751 24 Uppsala, Sweden and the [§]Department of Molecular Biology, Swedish University of Agricultural Sciences, Biomedical Center, Box 590, SE-751 24 Uppsala, Sweden

Isopentenyl diphosphate is the precursor of various isoprenoids that are essential to all living organisms. It is produced by the mevalonate pathway in humans but by an alternate route in plants, protozoa, and many bacteria. 1-Deoxy-D-xylulose-5-phosphate reductoisomerase catalyzes the second step of this non-mevalonate pathway, which involves an NADPH-dependent rearrangement and reduction of 1-deoxy-D-xylulose 5-phosphate to form 2-C-methyl-D-erythritol 4-phosphate. The use of different pathways, combined with the reported essentiality of the enzyme makes the reductoisomerase a highly promising target for drug design. Here we present several high resolution structures of the *Mycobacterium tuberculosis* 1-deoxy-D-xylulose-5-phosphate reductoisomerase, representing both wild type and mutant enzyme in various complexes with Mn^{2+} , NADPH, and the known inhibitor fosmidomycin. The asymmetric unit corresponds to the biological homodimer. Although crystal contacts stabilize an open active site in the B molecule, the A molecule displays a closed conformation, with some differences depending on the ligands bound. An inhibition study with fosmidomycin resulted in an estimated IC_{50} value of 80 nM. The double mutant enzyme (D151N/E222Q) has lost its ability to bind the metal and, thereby, also its activity. Our structural information complemented with molecular dynamics simulations and free energy calculations provides the framework for the design of new inhibitors and gives new insights into the reaction mechanism. The conformation of fosmidomycin bound to the metal ion is different from that reported in a previously published structure and indicates that a rearrangement of the intermediate is not required during catalysis.

Within the non-mevalonate pathway (1, 2), present in plants, protozoa, green algae, and many bacteria (1–3), pyruvate and D-glyceraldehyde 3-phosphate are used for the production of

isopentenyl diphosphate. Isopentenyl diphosphate in turn is the precursor of vital isoprenoids, such as steroid hormones, carotenoids, cholesterol, and ubiquinone (4). In eukaryotes and Archaea (5) isopentenyl diphosphate is instead formed through the mevalonate pathway (6) starting from acetyl-CoA. The fact that humans use a different route from plants, protozoa, and many bacteria for the formation of isopentenyl diphosphate combined with the essentiality of isoprenoids makes all the enzymes within the non-mevalonate pathway interesting as potential targets for drugs and herbicides.

Tuberculosis is one of the most serious diseases of our times. According to the World Health Organization, the causative bacterium, *Mycobacterium tuberculosis*, currently infects one-third of the world population, resulting in two million deaths annually. The increased prevalence of drug-resistant and multidrug-resistant strains together with the lethal combination that tuberculosis and AIDS represents, makes the need for new and better drugs urgent. In the search for new potential drug targets a number of aspects have to be considered. For instance, the target enzyme should perform a reaction vital for the bacteria, and if possible it should not have any human homologues. All enzymes within the non-mevalonate pathway fulfill these and other requirements and are, therefore, potential drug targets in *M. tuberculosis*.

1-Deoxy-D-xylulose-5-phosphate reductoisomerase (DXR,² also referred to as IspC; EC 1.1.1.267) catalyzes the NADPH-dependent rearrangement and reduction of 1-deoxy-D-xylulose 5-phosphate (DXP) to form 2-C-methyl-D-erythritol 4-phosphate (MEP) as the second step in the non-mevalonate pathway. The reaction requires the presence of a divalent cation such as Mg^{2+} , Co^{2+} , or Mn^{2+} (7). All the enzymes within the non-mevalonate pathway in *Bacillus subtilis* have been shown to be essential (8), and knockouts of the DXR enzyme in *Escherichia coli* (7, 9) are lethal. The essentiality of DXR in *M. tuberculosis* has also recently been demonstrated.³

Fosmidomycin is a known inhibitor of the non-mevalonate pathway in plants and bacteria (10) and has been shown to

* This work was supported by funding from the Foundation for Strategic Research, the Swedish Research Council, the European Union Sixth Framework Program NM4TB CT:018923, and by Uppsala University. The costs of publication of this article were defrayed in part by the payment of page charges. This article must therefore be hereby marked "advertisement" in accordance with 18 U.S.C. Section 1734 solely to indicate this fact.

The atomic coordinates and structure factors (code 2JCV, 2JCX, 2JCY, 2JCZ, 2JD0, 2JD1, and 2JD2) have been deposited in the Protein Data Bank, Research Collaboratory for Structural Bioinformatics, Rutgers University, New Brunswick, NJ (<http://www.rcsb.org/>).

¹ To whom correspondence should be addressed. Tel.: 46-18-4714982; Fax: 46-18-536971; E-mail: Alwyn@xray.bmc.uu.se.

² The abbreviations used are: DXR, 1-deoxy-D-xylulose-5-phosphate reductoisomerase; DXP, 1-deoxy-D-xylulose 5-phosphate; EcDXR, DXR from *E. coli*; F, fosmidomycin; M, Mn^{2+} ; MEP, 2-C-methyl-D-erythritol 4-phosphate; MD, molecular dynamics; MtDXR, DXR from *M. tuberculosis*; N, NADPH; S, sulfate; ESRF, European Synchrotron Radiation Facility; Bis-Tris, 2-[bis(2-hydroxyethyl)amino]-2-(hydroxymethyl)propane-1,3-diol; PDB, Protein Data Bank.

³ A. Brown and T. Parish, personal communication.

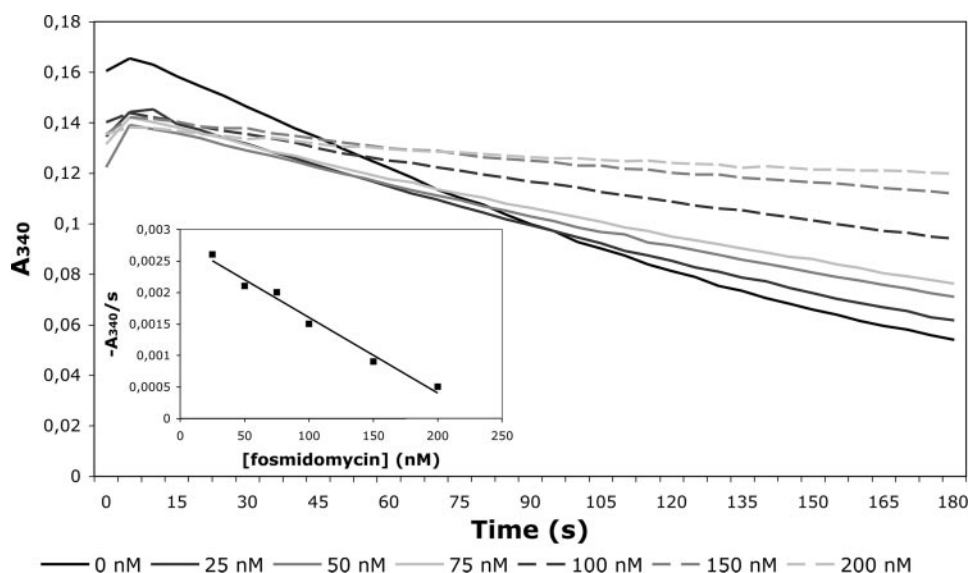


FIGURE 1. **Inhibition of *MtDXR* by fosmidomycin.** The inhibitory capacity of fosmidomycin was evaluated in a spectrophotometric assay, in which the *MtDXR*-catalyzed NADPH-dependent rearrangement and reduction of DXP to form MEP is monitored at 340 nm. The inset shows the relationship between the change in absorbance per second, $\Delta A_{340} \text{ s}^{-1}$, and the fosmidomycin concentration, for those reactions containing the inhibitor. The reaction rate in the absence of fosmidomycin was $0.0036 \Delta A_{340} \text{ s}^{-1}$.

specifically inhibit DXR (11, 12). The compound is active against the protozoan parasite *Plasmodium falciparum* in humans (13, 14) and *Plasmodium vinckei* in mice (15).

We have recently solved the structure of the *M. tuberculosis* DXR with a sulfate ion bound at the site of the phosphate moiety of the substrate DXP (16), which is available in the Protein Data Bank (17) under accession code 2C82. In the PDB, 12 other DXR structures are currently available representing enzymes from *E. coli* (18–22) and *Zymomonas mobilis* (23). Among the *E. coli* DXR (*EcDXR*) entries are two apo structures (PDB codes 1K5H and 1ONN) (18, 19), one structure in complex with the inhibitor fosmidomycin and a Mn^{2+} ion (PDB code 1ONP) (19), and one in complex with NADPH and the substrate DXP (PDB code 1Q0Q) (21). The two *Z. mobilis* entries represent structures in complex with an acetate ion and NADPH, respectively. In this paper only the *EcDXR* structures will be discussed because they provided by far the most complete view of DXR structure and function.

Here we report a new cloning, expression, and purification procedure for the *M. tuberculosis* DXR (*MtDXR*), Rv2870c (24) that makes this target more amenable to structural analysis. Kinetic studies of this new construct explore the inhibition of the enzyme with fosmidomycin together with the properties of a double mutant containing the mutations D151N and E222Q (*MtDXR*^{NQ}). We also report the x-ray structures of *MtDXR* in four different complexes: fosmidomycin, Mn^{2+} , and NADPH; fosmidomycin and NADPH; Mn^{2+} , NADPH, and SO_4^{2-} ; Mn^{2+} and SO_4^{2-} . Structures of *MtDXR*^{NQ} are also reported in three complexes: SO_4^{2-} ; NADPH and SO_4^{2-} ; fosmidomycin and NADPH. These structures and the information they provide contribute to an improved understanding of the reaction mechanism catalyzed by *MtDXR* and also to the development of new inhibitors.

EXPERIMENTAL PROCEDURES

Cloning, Protein Expression, and Purification—The sequence corresponding to *MtDXR* (Rv2870c, originating from *M. tuberculosis* strain H37R (24)) amino acids 1–389 (of 413 in the full-length protein, molecular mass 41.7 kDa) was amplified by PCR from a previous construct (16). The primers 5'-CACCATTGGCTCATCATCATCATCATCATGTGACCAACTCG-ACCGAC-3' (forward) and 5'-CTACATACCAGATACCGCGCGCTG-3' (reverse), used together with *Pfu* Ultra DNA polymerase (Stratagene), simultaneously introduced an N-terminal His₆ tag. The Champion™ pET101 Directional TOPO® expression kit (Invitrogen) was used for ligation of the PCR product into the pET101D-TOPO vector.

The primers 5'-GTCAGATCGTGCCGGTCAACTCCGAACAC-TCCGCGCTG-3' (D151N) and 5'-CTGGTCAACAAGGGA-CTTCAGGTCATCGAAACCCACCTG-3' (E222Q) used with the QuikChange mutagenesis kit (Invitrogen) introduced the replacements of the *MtDXR* double mutant, *MtDXR*^{NQ}, using the new *MtDXR* clone as template.

Cloning for both *MtDXR* and *MtDXR*^{NQ} was performed in *E. coli* TOP10F' cells (Invitrogen). Positive clones were selected for by growth on Luria agar plates containing 50 $\mu\text{g}/\text{ml}$ ampicillin, and plasmids were isolated after the QIAprep® Spin Miniprep kit protocol (Qiagen). For *MtDXR*, an analytical PCR was performed using the T7 forward primer from the Champion™ pET101 Directional TOPO® expression kit (Invitrogen) and the reverse primer. For *MtDXR*^{NQ} the analytical PCR was performed using the T7 reverse primer, and the analytical primers 5'-GTCAGATCGTGCCGGTCA-3' and 5'-CTGGTCAACAAGGGA-CTTC-3'. The clones were verified by DNA sequence analysis (Uppsala Genome Center, Rudbeck Laboratory). Expression was carried out in *E. coli* BL21-STAR™ (DE3) cells (Invitrogen) at 37 °C. The cultures were induced with 100 mg/liter isopropyl- β -D-thiogalactopyranoside (Sigma) at an $A_{550} = 0.6$, and growth was continued for 3 h. The cells were harvested and washed with 1× SSPE buffer (150 mM NaCl, 10 mM NaH_2PO_4 , pH 7.5, 1 mM EDTA), then stored at –20 °C.

Purification followed the previous protocol (16) with the following modifications. After purification on a nickel-NTA column (Qiagen), the buffer was replaced on a PD10 column (GE Healthcare) with one containing 150 mM NaCl, 10% glycerol, and 20 mM Tris-HCl, final pH 7.5. The protein was further purified by size exclusion chromatography on a HiLoad™ 16/60 Superdex™ 200 column (Amersham Biosciences) developed with the same buffer.

The pooled fractions were concentrated to 4.3 mg/ml, and the glycerol concentration was at the same time lowered to 2%.

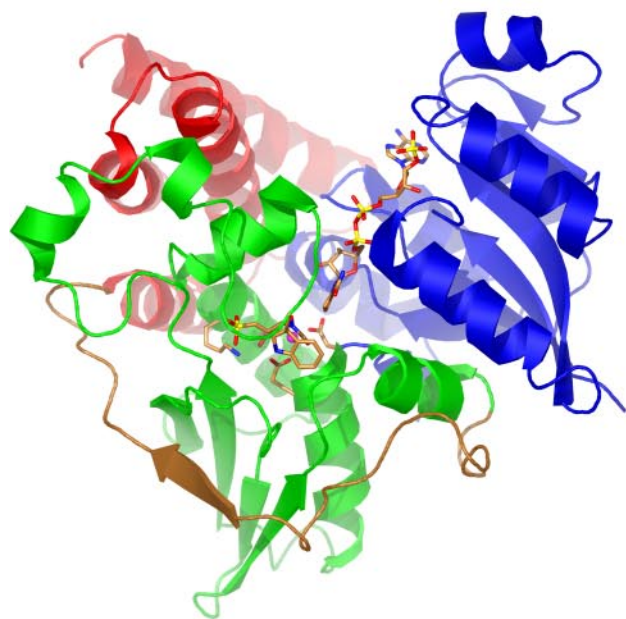
TABLE 1**Data collection and refinement statistics**

Values in parenthesis are for the highest resolution shell.

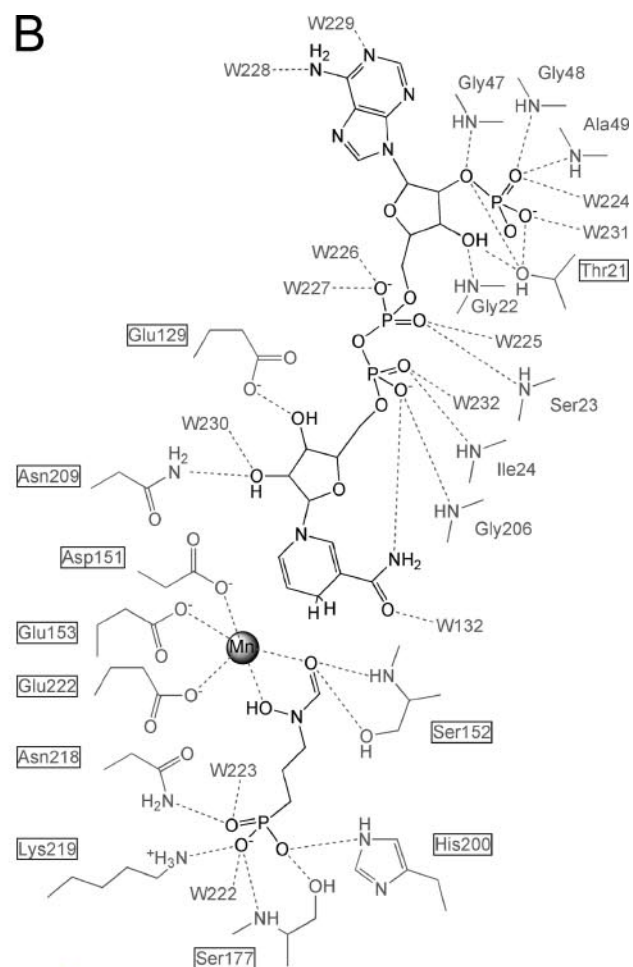
	<i>MtDXR</i> -MS	<i>MtDXR</i> -MNS	<i>MtDXR</i> -FN	<i>MtDXR</i> -FMN	<i>MtDXR</i> ^{NO} -S	<i>MtDXR</i> ^{NO} -NS	<i>MtDXR</i> ^{NO} -FN
Data collection statistics							
Beam line	1911-2, MAX-lab	ID14-2, ESRF	ID14-4, ESRF	ID14-3, ESRF	1911-2, MAX-lab	ID14-2, ESRF	ID14-4, ESRF
Wavelength (Å)	67.59 64.81 85.96	67.33 64.89 86.06	67.35 65.48 86.09	67.28 65.26 86.04	68.11 64.82 86.33	67.63 65.61 86.02	67.61 65.32 86.18
Cell axial lengths (Å)	90.0 101.9 90.0	90.0 101.7 90.0	90.0 101.6 90.0	90.0 101.8 90.0	90.0 101.7 90.0	90.0 102.0 90.0	90.0 101.9 90.0
Cell angles (°)	P2 ₁	P2 ₁	P2 ₁	P2 ₁	P2 ₁	P2 ₁	P2 ₁
Space group	35.00-2.15 (2.27-2.15)	35.00-2.00 (2.11-2.00)	30.00-2.20 (2.32-2.20)	30.00-2.05 (2.16-2.05)	40.00-2.35 (2.48-2.35)	35.00-2.30 (2.42-2.30)	30.00-2.10 (2.21-2.10)
Resolution range (Å)	152,495	226,619	135,226	141,985	126,833	148,670	171,156
Number of reflections measured	39,797	49,295	36,913	45,559	30,603	32,964	42,772
Number of unique reflections	3.8 (3.8)	4.6 (4.6)	3.7 (3.4)	3.1 (3.1)	4.1 (3.6)	4.5 (4.5)	4.0 (3.5)
Average multiplicity	100.0 (100.0)	100.0 (100.0)	98.5 (91.5)	99.2 (99.9)	99.0 (93.1)	100.0 (100.0)	99.3 (96.2)
Completeness (%)	0.077 (0.236)	0.116 (0.475)	0.090 (0.266)	0.134 (0.514)	0.074 (0.191)	0.102 (0.431)	0.068 (0.195)
<i>R</i> _{meas} ^a	16.2 (6.3)	12.4 (3.3)	13.8 (6.0)	9.8 (3.0)	17.5 (6.9)	13.4 (3.5)	16.7 (7.0)
(1)/(σ _t)							
Refinement statistics							
Resolution range (Å)	35.00-2.15 (2.21-2.15)	35.00-2.00 (2.05-2.00)	30.00-2.20 (2.26-2.20)	30.00-2.05 (2.10-2.05)	40.00-2.35 (2.41-2.35)	35.00-2.30 (2.36-2.30)	30.00-2.10 (2.15-2.10)
Number of reflections used in working set	37,758 (2,767)	46,754 (3,407)	35,057 (2,149)	43,246 (3,200)	29,050 (1,911)	31,255 (2,285)	40,602 (2,774)
Number of reflections for <i>R</i> _{free} calculation	1,996 (140)	2,493 (181)	1,848 (121)	2,297 (175)	1,540 (86)	1,672 (117)	2,156 (117)
<i>R</i> (%)	17.9 (19.3)	17.7 (20.7)	16.3 (17.2)	17.7 (21.2)	18.3 (19.3)	20.2 (23.4)	18.0 (19.6)
<i>R</i> _{free} (%)	22.5 (27.4)	22.1 (26.0)	20.9 (26.8)	22.4 (28.0)	23.6 (31.6)	25.5 (32.8)	21.5 (25.7)
Number of non-hydrogen atoms	5,986	6,178	6,225	6,174	5,933	5,886	6,114
Number of solvent waters	388	507	521	502	327	263	440
Mean B-factor, protein atoms (Å ²)	23.2, 17.5	17.9, 15.0	15.8, 16.9	16.7, 17.1	22.6, 17.4	31.7, 26.0	23.2, 20.2
Mean B-factor, solvent atoms (Å ²)	24.4	23.7	24.1	24.7	21.7	26.8	28.2
Mean B-factor, fosmidomycin (Å ²)			14.8	15.5			33.8
Mean B-factor, NADPH (A, B) (Å ²)		31.5	18.8, 26.6	16.8, 40.1 ^b		56.1 ^b	32.1 ^b , 40.9 ^b
Mean B-factor, Mn ²⁺ (Å ²)	29.3, 15.3	16.0, 9.4	12.7, 11.5	12.7, 11.5			
Mean B-factor, sulfate ligands (A, B, AB) (Å ²)	24.2, 15.6, 23.2	16.5, 11.3, 22.9	–, 23.1, 28.6	–, 13.0, 22.1	24.4, 27.8, 29.8	33.0, 30.2, 37.8	–, 30.8, 25.8
Ramachandran plot outliers (%) ^c	1.3	0.9	0.6	1.2	1.5	1.2	0.9
Root mean square deviation from ideal bond length (Å) ^d	0.010	0.010	0.012	0.010	0.008	0.008	0.011
Root mean square deviation from ideal bond angle (°) ^d	1.16	1.17	1.23	1.20	1.10	1.11	1.27

^a Multiplicity-corrected *R*_{meas} (57).^b Calculated on the part of NADPH with full occupancy.^c Calculated using a strict-boundary Ramachandran plot (58).^d Calculated using small molecule-based parameters (59).

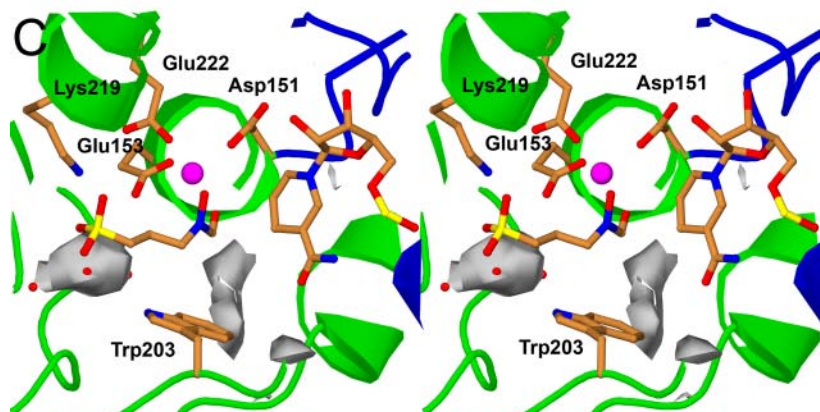
A



B



C



D

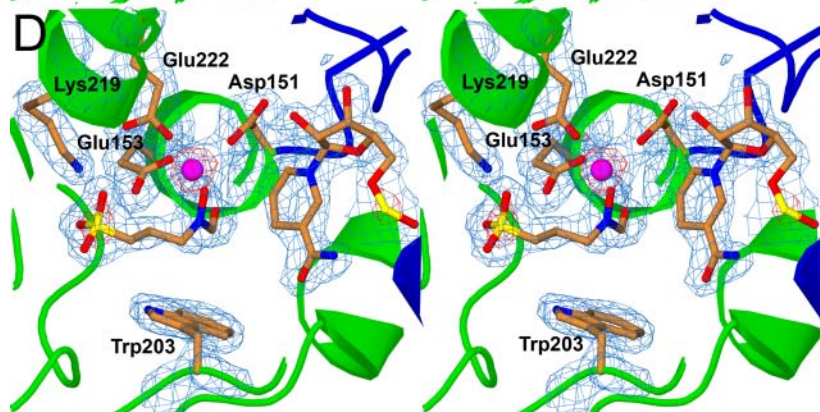


TABLE 2

Distances across the active site of *M. tuberculosis* (between residues 47 and 339) and *E. coli* (between residues 36 and 348) DXR structures

For the first seven structures listed below (*Mt*DXR-MS, *Mt*DXR-MNS, *Mt*DXR-FN, *Mt*DXR-FMN, *Mt*DXR^{NQ}-S, *Mt*DXR^{NQ}-NS, and *Mt*DXR^{NQ}-FN), the average distance in the A and B chains was 21.0 ± 0.7 Å and 24.7 ± 0.2 Å, respectively.

Structure	PDB entry code	Distance in A chain	Distance in B chain	Reference
		Å	Å	
<i>Mt</i> DXR-MS	2JD2	21.5	24.6	This work
<i>Mt</i> DXR-MNS	2JD1	20.7	24.6	This work
<i>Mt</i> DXR-FN	2JCV	20.3	24.8	This work
<i>Mt</i> DXR-FMN	2JCZ	20.3	25.0	This work
<i>Mt</i> DXR ^{NQ} -S	2JCY	22.3	24.9	This work
<i>Mt</i> DXR ^{NQ} -NS	2JD0	21.4	24.5	This work
<i>Mt</i> DXR ^{NQ} -FN	2JCX	20.7	24.8	This work
<i>Mt</i> DXR-S	2C82	22.5	22.5	16
<i>Ec</i> DXR (A-A' dimer)	1K5H	28.0 (A chain)	28.0 (A' chain)	18
<i>Ec</i> DXR (B-C dimer)	1K5H	28.0 (B chain)	26.1 (C chain)	18
<i>Ec</i> DXR	1ONN	25.9	25.9	19
<i>Ec</i> DXR-S	1T1R	24.5	24.4	22
<i>Ec</i> DXR-M	1ONO	25.0	25.1	19
<i>Ec</i> DXR-MS	1T1S	24.5	24.6	22
<i>Ec</i> DXR-FM	1ONP	25.4	25.4	19
<i>Ec</i> DXR-NS	1JVS	24.7	24.6	20
<i>Ec</i> DXR-FN	1QOL	18.4		21
<i>Ec</i> DXR-FN, citric acid	1QOH	18.4		21
<i>Ec</i> DXR-N,DXP	1QOQ	17.6	18.1	21

The material was more than 98% pure as deduced from SDS/PAGE analysis (PhastSystemTM, Amersham Biosciences). The yield of pure protein was 1.4 mg/liter culture for *Mt*DXR and 1.7 mg/liter culture for *Mt*DXR^{NQ}.

Inhibition Assay—DXP and fosmidomycin were generously provided by AstraZeneca India Pvt. Ltd. The inhibitory potential of fosmidomycin was evaluated in a spectrophotometric assay (7, 25) in which the NADPH-dependent rearrangement and reduction of DXP to form MEP, catalyzed by *Mt*DXR, was monitored at 340 nm using the absorption of NADPH ($\epsilon_{340} \text{ nm} = 6220 \text{ M}^{-1} \text{ cm}^{-1}$). Each assay contained 350 μl of reaction buffer (129 mM NaCl, 2.9 mM β -mercaptoethanol, 5.7% Me₂SO, 2.1 mM MnCl₂, and 64 mM HEPES-NaOH, pH 7.5), 50 μl of 3.85 μM *Mt*DXR (in 100 mM NaCl, 0.01% Brij-35, and 50 mM HEPES-NaOH pH 7.5), 50 μl of 1.1 mM NADPH (in distilled H₂O), 50 μl of 2.2 mM DXP (in distilled H₂O), and 50 μl of fosmidomycin (in distilled H₂O).

One measurement was made in the absence of fosmidomycin together with six measurements with final fosmidomycin concentrations ranging between 25 and 200 nM. The decrease in absorbance at 340 nm was followed at 22 °C (DU® 640 spectrophotometer, Beckman) with time points every 5 s during a 3-min period. The slope of the linear phase (25–125 s) of each reaction was used in calculating the initial velocity (Fig. 1). The velocities were plotted against the corresponding fosmidomycin concentrations. A line was fitted to the points in the approximately linear region of the curve (*inset* in Fig. 1), and the equa-

tion so generated was used to estimate the IC₅₀ value of fosmidomycin.

Crystallization—*Mt*DXR was co-crystallized with fosmidomycin using vapor diffusion. The sitting drop contained 0.9 μl of protein solution (3.3 mg/ml *Mt*DXR in the buffer used during concentration, plus 10 mM fosmidomycin, 3 mM NADPH, 0.1 mM EDTA, and 10 mM dithiothreitol) and 0.9 μl of reservoir solution (0.2 M AmSO₄, 25% polyethylene glycol 3350, and 0.1 M Bis-Tris, final pH 5.7) at 22 °C. Needle-like crystals appeared within a few days. Crystallization of both *Mt*DXR and *Mt*DXR^{NQ} was then optimized with the aid of seeding in a batch experiment. The 4- μl sitting drops consisted of 2 μl of protein solution (3.3 mg/ml *Mt*DXR or *Mt*DXR^{NQ} in the buffer used in the concentration with the addition of 0.1 mM EDTA and 10 mM dithiothreitol) and 2 μl of crystallization buffer (0.2 M AmSO₄, 25% polyethylene glycol 3350, and 0.1 M Bis-Tris, final pH 5.7). The reservoir solution consisted of 0.1 M AmSO₄, 12.5% polyethylene glycol 3350, 0.05 M Bis-Tris, 75 mM NaCl, and 10 mM Tris-HCl, final pH 5.9.

*Mt*DXR was co-crystallized with ligands in the combinations: DXP and MnSO₄; DXP and NADPH; DXP, MnSO₄ and NADPH; fosmidomycin and NADPH; fosmidomycin, MnSO₄, and NADPH. The mutant *Mt*DXR^{NQ} was crystallized without ligands as well as in the following combinations: DXP, MnSO₄, and NADPH; fosmidomycin and NADPH. The following concentrations of the ligands were added to the protein solution in co-crystallization experiments: 20 mM DXP, 10 mM fosmidomycin, 12 mM MnSO₄, and 3 mM NADPH. Needle-like crystals appeared within a few days and grew to average dimensions of $0.2 \times 0.05 \times 0.02$ mm in 2 weeks. Before the crystals were flash-cooled in liquid nitrogen, they were transferred to a drop of cryo solution containing 0.1 M AmSO₄, 13% polyethylene glycol 3350, 0.06 M Bis-Tris, 75 mM NaCl, 25% glycerol, final pH 5.7. Depending on which ligands were used for co-crystallization, the following concentrations of the ligands were also present in the cryo solution: 10 mM DXP, 10 mM fosmidomycin, 12 mM MnSO₄, and 3 mM NADPH.

Data Collection, Structure Determination, Refinement, and Analysis—X-ray data were collected under cryo conditions at various beamlines at the European Synchrotron Radiation Facility (ESRF) in Grenoble, France, and at MAX-lab in Lund, Sweden (Table 1). Diffraction data were indexed and integrated with MOSFLM (26) and processed with SCALA (27) as implemented in the CCP4 program suite (28). Statistics are shown in Table 1. The crystals possessed the symmetry of space group P2₁. The Matthews coefficient (29) suggested that there were two molecules in the asymmetric unit; the value was predicted to be $2.2 \text{ Å}^3/\text{Da}$ with 44.5% solvent. The structures were solved by molecular replacement using AMoRe (30) with the apo *M. tuberculosis* DXR structure (PDB code 2C82) (16) as a search

FIGURE 2. Structure of *Mt*DXR-FMN. A, the position of NADPH in the N-terminal domain (blue) and of fosmidomycin and the Mn²⁺ ion underneath the active site flap in the catalytic domain (green) are shown. Shown also are the side chains of residues Asp-151, Glu-153, and Glu-222 (which interact with the metal ion) as well as of Lys-219 (which interacts with the phosphonate moiety of the inhibitor) and Trp-203 (which is positioned in the active site flap and stacks on the inhibitor). B, hydrogen bonding interactions to and between the Mn²⁺ ion, fosmidomycin, and NADPH in the active site. C, stereo view illustrating the pockets close to the active site of *Mt*DXR-FMN. The larger pocket contains four water molecules, of which three are visible in this view as small red spheres. The calculation was performed with the *asa* command in O using a probe with a radius of 1.2 Å and a model lacking water molecules. D, stereo view showing the electron density in the active site of *Mt*DXR-FMN. The SIGMAA-weighted $(5\sigma) 2|F_o| - |F_c|$ map was contoured at 1σ (blue, 0.4 e/Å^3) and 5σ (red, 2.0 e/Å^3).

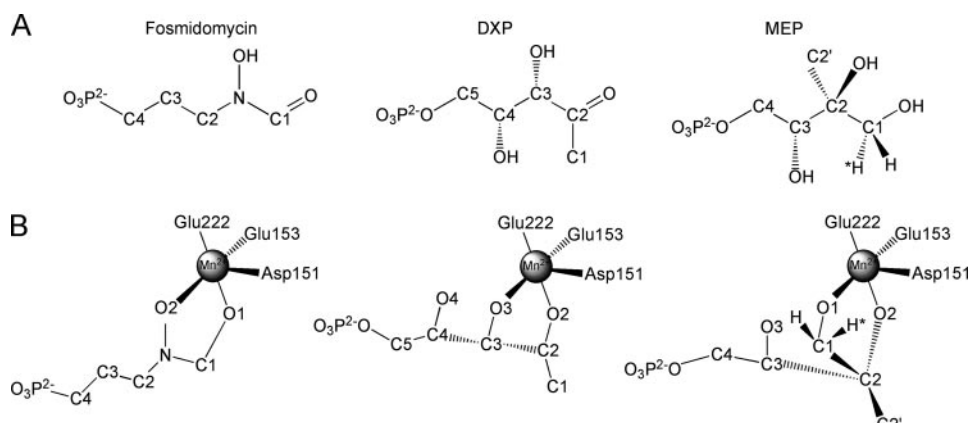


FIGURE 3. **Fosmidomycin, DXP, and MEP.** A, carbon atom numbering of fosmidomycin, DXP, and MEP. B, the conformation of fosmidomycin around the metal ion is illustrated as well as the modeled conformations of DXP and MEP. The H* hydrogen at C1 of MEP is derived from the NADPH cofactor. In our proposal the O3 and O2 atoms of the substrate remain coordinated to the active site ion, becoming the O1 and O2 hydroxyl groups of the product without substantial rearrangement.

model. Refinement was carried out with the program REFMAC5 (31), and rebuilding was performed with the program O (32). Waters were added after analyzing the results from the ARP/wARP (33) water-building routine. Different weights were tested in the refinement to find the best combinations of R_{free} and stereochemistry. Final refinement statistics are shown in Table 1.

Structural comparisons were made with the *lsq* commands in O using a 3.8-Å paired distance cut-off. The initial coordinates for DXP were taken from the *E. coli* DXP/NADPH complex (PDB code 1Q0Q) (21) after superposition onto the *Mt*DXR structure in complex with fosmidomycin, Mn²⁺, and NADPH. The DXP was then docked interactively to optimize the overlap with our experimental fosmidomycin structure. MEP was then generated from the DXP model, maintaining the Mn²⁺ coordination. We consider the models of DXP/MEP shown in Fig. 4D to be good working hypotheses for the mode of ligand binding in each case. Figs. 2, A, C, and D, and 4 were made in O and rendered in MOLRAY (34). Figs. 2B and 3 were prepared with ChemDraw (CambridgeSoft Corp.).

Docking, Molecular Dynamics, and Empirical Valence Bond Calculations—The free energy profile for proton abstraction from the O4 hydroxyl of DXP by the carboxylate group of Glu-153 (see “Discussion”) was investigated using the empirical valence bond method (35, 36). Molecular dynamics (MD) simulations combined with the free energy perturbation technique was used to drive the reaction from one valence bond state to the other while evaluating the reaction free energy profile by umbrella sampling. The uncatalyzed reaction free energy surface in water was first calibrated by adjusting the gas phase free energy difference, $\Delta\alpha_{ij}$, and the off-diagonal matrix elements, H_{12} , between pairs of valence bond states, and these parameters were then used to describe the corresponding process in the solvated protein-substrate complex (35, 36). The valence bond states used here correspond to the negatively charged carboxylate of Glu-153 and the O4 hydroxyl of DXP (ϕ_1) and to the protonated carboxylate of Glu-153 and the charged O4 alkoxide anion of DXP (ϕ_2). For DXP, restrained electrostatic potential (37) charges were derived for all atoms except for the dian-

ionic phosphate group, for which partial charges were extracted from the CHARMM22 force field (38). From the pK_a difference between the O4 hydroxyl of DXP and glutamic acid, the reaction free energy for the proton abstraction in water, $\Delta G^{\circ}_{\text{wat}}$, was estimated to be 14.3 kcal/mol. The corresponding activation free energy, $\Delta G^{\ddagger}_{\text{wat}}$, was predicted from linear free energy relationships to be 15.4 kcal/mol after correction for bringing the donor and acceptor to contact distance (39, 40).

The docking calculations and MD simulations were carried out based on the *M. tuberculosis* DXR structure in complex with fosmidomycin, Mn²⁺, and NADPH.

The binding mode of DXP was modeled with the program GOLD Version 3.0 using default settings and 50 docking runs (41). The top-ranked solution was essentially identical to the interactively docked DXP. In the MD simulation of the reaction, we used the *Mt*DXR structure in complex with NADPH, the docked DXP, and an active site Mg²⁺ ion, which was placed in the same position as the Mn²⁺ ion in the original structure. The complex was solvated by using TIP3P water molecules (42) in a sphere with a 24-Å radius centered on DXP.

The MD/free energy perturbation/empirical valence bond calculations were carried out with the program Q (43) using the Amber95 force field (44). For NADPH, slightly modified restrained electrostatic potential partial charges were used (45). The simulations were carried out in a sphere with a 24-Å radius using a previously described MD protocol (46). The free energy perturbation calculation was then carried out in 51 discrete steps with a 5-ps trajectory generated at each step. Energies were saved every 5 fs, and in the empirical valence bond calculations the first 2 ps of each file were discarded for equilibration.

RESULTS

Enzyme Properties—The shortened construct used was designed based on observations in the previous apo structure (16), where the last four residues of the construct (390–393) could not be observed in the electron density. The protein with an N-terminal His₆ tag was overexpressed in *E. coli*. It behaved as a homogenous dimer during purification, and the activity was similar to that reported for the previous construct. A mutant protein, *Mt*DXR^{NQ}, containing the substitutions D151N and E222Q, was also expressed; this double mutant showed no activity. To test the inhibitory capacity of fosmidomycin, the NADPH-dependent rearrangement and reduction of DXP to form MEP was evaluated using a spectrophotometric assay; see Fig. 1. With *Mt*DXR at a concentration of 0.35 μM and substrate concentrations of 0.2 mM for DXP and 0.1 mM for NADPH, the IC₅₀ value of fosmidomycin was estimated to be 80 nM.

MtDXR and MtDXR^{NQ} Structures—The MtDXR and MtDXR^{NQ} complex structures were solved in space group P2₁ by molecular replacement using the apo MtDXR structure as a search model. The various structures were refined to resolutions ranging between 2.00 and 2.35 Å; data collection and refinement statistics are summarized in Table 1. The asymmetric unit in each case contains one homodimer. Unless otherwise indicated, the electron density for the main chain was of very good quality except for the N-terminal His₆ tag and the first 10 residues. The subunit is, as previously described, composed of three domains, an N-terminal NADPH binding domain, a central catalytic domain, and a C-terminal α -helical domain. The domains are arranged in a V shape, where the N-terminal and C-terminal domains form the two arms, and the catalytic domain lies at the vertex (Fig. 2A). The dimer interface is created by interactions between the catalytic domains and the connecting regions that lie between the catalytic and the C-terminal domain of each subunit. A sulfate ion is also placed close to the dimer interface interacting with the side chain of Arg-162 (NE and NH₂) from the A molecule.

During refinement of the structures crystallized in the presence of DXP, it became clear that the substrate could not be modeled in any of the structures. Instead, a sulfate ion was found in the active site at the expected position of the DXP phosphate. Therefore, the structures presented in this paper are designated as MtDXR-FMN, MtDXR-FN, MtDXR-MNS, MtDXR-MS, MtDXR^{NQ}-S, MtDXR^{NQ}-NS, and MtDXR^{NQ}-FN (where F stands for fosmidomycin, M for Mn²⁺, N for NADPH, and S for SO₄²⁻).

The root mean square difference between C α positions in the two subunits when they are superimposed ranges between 1.6 and 2.0 Å in the different structures. The rather large values reflect significant conformational differences between the two subunits, as was also observed for the first published DXR structure (*Ec*DXR, PDB code 1K5H). The differences are best described as rigid body domain rotations combined with flexibility of the active site flap (residues 198–209). In the B molecule the flap is locked into an open conformation by crystal packing interactions, which results in poor or no electron density for inhibitor or cofactor. By contrast, the conformations of the active site flap in the A molecules depend on the interactions with substrates, cofactors, and inhibitors and are linked to well defined ligand electron density; thus, most of the discussion that follows will focus on the active site of the A molecule.

When aligning the dimers (C α positions) of the seven *M. tuberculosis* structures presented here using a restrictive pair cutoff of 0.5 Å, one can see that the complete B chains and dimer-forming central catalytic domain of the A chains are well aligned. This indicates that the crystal contacts keep the B chains fixed while allowing the A chains to flex depending on the ligand state. Using the distance across the active site cleft (between the C α atoms of residues Gly-47 and Ala-339) as a simple yardstick, the relative motions of the N- and C-terminal domains can be assessed (Table 2). The S.D. for this distance is 0.7 Å for the A chains but only 0.2 Å for the B chains. Furthermore, the A chains that bind NADPH show similar, more closed conformations, whereas the other A chains from the

mutant and from the structure lacking NADPH show a larger variation and also a larger separation across the active site cleft.

MtDXR-MS displays octahedral coordination of the Mn²⁺ ions, each of which interacts with three water molecules and the *syn* orbitals of residues Asp-151 (OD1 and OD2, respectively, in A and B), Glu-153 (OE1), and Glu222 (OE1). The sulfate ion interacts with three water molecules and with residues Ser-177 (OG and N), Ser-213 (OG), Asn-218 (ND2), and Lys-219 (NZ), which are conserved residues in DXR sequences (47) and make up a phosphate/phosphonate binding pocket that has been described in *Ec*DXR-N,DXP and *Ec*DXR-FN. Poor electron density is observed for residues A199–A206 and B204–B206 in the active site flap regions.

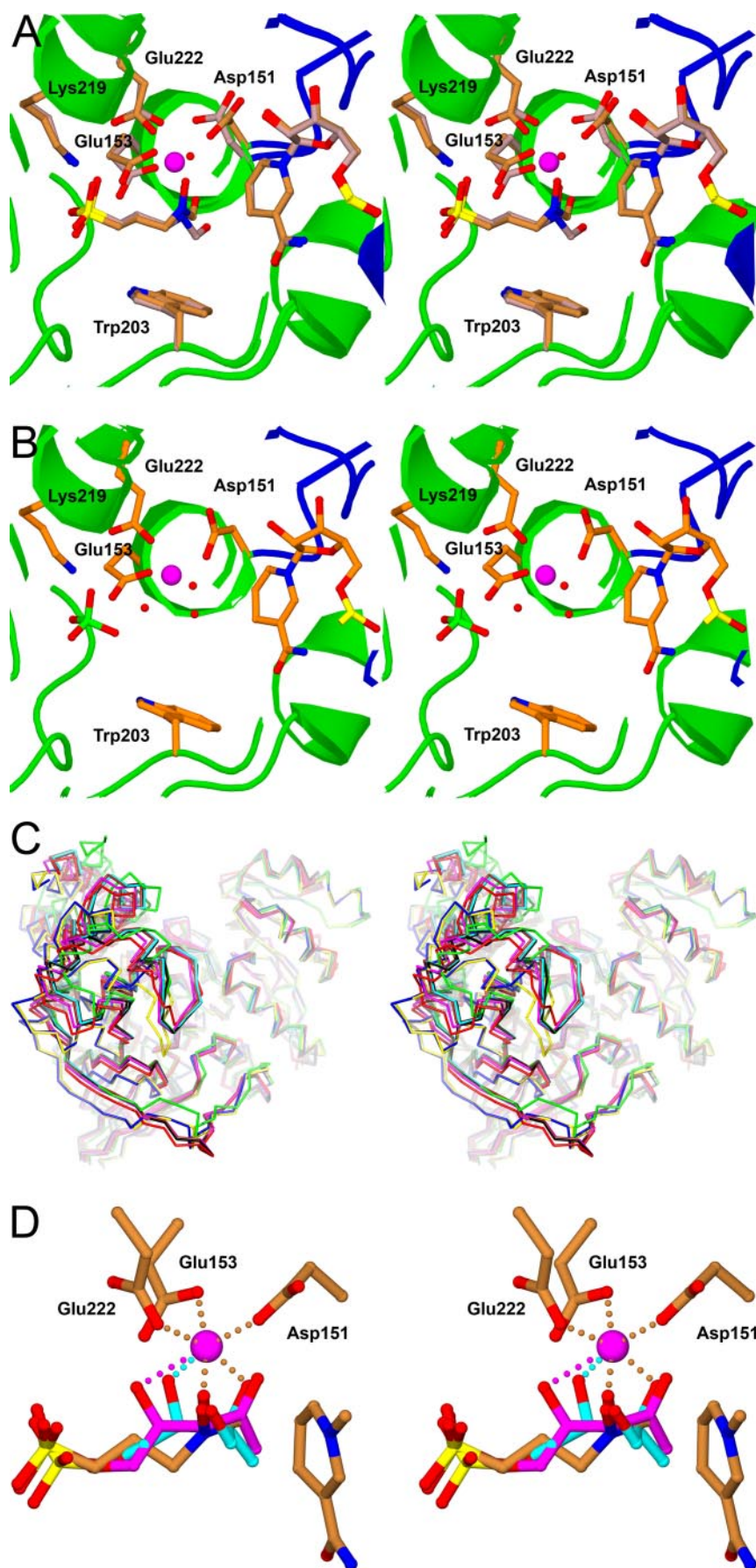
The MtDXR-MNS structure shows that the binding of NADPH has little effect on the Mn²⁺ coordination. However, the interactions with the sulfate ion are affected by NADPH binding, albeit indirectly. The flap of the A molecule is better defined than for the MtDXR-MS structure, with improved density for the imidazole ring of His-200, which interacts with the sulfate via NE2. However, the temperature factors of key flap side chains are still somewhat elevated (in the range of 30–40 Å²). The density for the nicotinamide ring and also for a portion of the sugar in the NADPH is also quite weak, with correspondingly high B-factors. The nicotinamide phosphate and AMP portion of the cofactor have better density and lower B-factors. In the B molecule, the metal ion and the sulfate are present, but the NADPH could not be modeled from the electron density (although some density is seen at the 2'-phosphate). Poor electron density is also observed for residues B204–B205.

MtDXR-FN shows clearly the position of fosmidomycin and NADPH in the absence of the Mn²⁺ ion. The electron density for the sugar and nicotinamide ring in the NADPH is better than that observed in MtDXR-MNS. Here only a small portion of the nicotinamide ring is mobile, indicating the importance of inhibitor and most probably also substrate binding for optimal binding of NADPH. The residues interacting with fosmidomycin are strictly conserved in *Ec*DXR-N,DXP, whereas only 70% of the residues interacting with NADPH in the *M. tuberculosis* structure are found in the *E. coli* enzyme. In the B molecule, a sulfate is bound at the phosphonate position of the inhibitor. Given the high concentration of AmSO₄ used in the crystallization, this is unlikely to be part of a disordered fosmidomycin molecule.

MtDXR-FMN provides the most complete picture of interactions in the active site of MtDXR (Fig. 2). NADPH is bound in the N-terminal domain and comes in close contact with the inhibitor fosmidomycin (closest contact is 3.1 Å from the C5 to O2 of the inhibitor; the naming convention is shown in Fig. 3A) and the Mn²⁺ ion that are positioned underneath the active site flap; see Fig. 2A. Residues Thr-21 (OG1), Gly-22 (N), Ser-23 (N), Ile-24 (N), Gly-47 (N), Gly-48 (N), Ala-49 (N), and Glu-129 (OE1) of the N-terminal domain interact with NADPH as well as residues Gly-206 (N) and Asn-209 (ND2) from the active site flap in the catalytic domain (Fig. 2B). The amine group of the Asn-209 side chain points directly at the center of the nicotinamide ring in a classic amide aromatic ring interaction (48). The Mn²⁺ ion is coordinated by interactions with residues Asp-151 (OD2), Glu-153 (OE1), and Glu-222 (OE2) as well as to the

Structures of *M. tuberculosis* DXR

inhibitor fosmidomycin (O1 and O2). The inhibitor also interacts with residues Ser-152 (OG and N), Ser-177 (OG and N), His-200 (NE2), Asn-218 (ND2), and Lys-219 (NZ), all located in the catalytic domain. The key side chains from the flap are well defined and cause the inhibitor to be completely shielded from the bulk solution. A number of solvent molecules, however, are trapped in an enclosed pocket (Fig. 2C), and one of these interacts with the phosphonate group. The electron density for the active site residues as well as for the Mn^{2+} ion, fosmidomycin, and NADPH is well defined (see Fig. 2D). When comparing *Mt*DXR-FMN with the most analogous *E. coli* DXR structure, that with PDB code 1ONP (19), it is evident that the coordination of the inhibitors around the Mn^{2+} ion is different. In *Mt*DXR-FMN one can see that when fosmidomycin binds, the octahedral coordination of the metal, as seen in *Mt*DXR-MNS and *Mt*DXR-MS, is slightly disturbed. Three water molecules are displaced. The two oxygen atoms of the (*N*-formyl-*N*-hydroxy) amino group of the inhibitor replace only two of these three water molecules, and so the sixth coordination site is empty. This may be a steric effect due to the lack of space between the C3 atom of the inhibitor and the OE2 of Glu-153. In the coordination seen in *Mt*DXR-FMN, the *N*-hydroxyl oxygen of the inhibitor, corresponding to the hydroxyl group at C3 in the DXP substrate (Fig. 3A), is positioned opposite Glu-153, in close proximity to C4 and C5 of the nicotinamide ring of NADPH (3.5 and 3.1 Å, respectively). The *N*-formyl oxygen, corresponding to O2 of the substrate, is positioned opposite residue Glu-222. Thus, the free coordination position is opposite Asp-151. By contrast, in 1ONP, the *N*-hydroxyl oxygen of fosmidomycin is positioned opposite the residue equivalent to Asp-151 in *Mt*DXR-FMN, whereas the *N*-formyl oxygen lies opposite the residue equivalent to Glu-222. A water



molecule positioned opposite the residue corresponding to Glu-153 completes the full octahedral coordination of the Mn^{2+} ion in the *E. coli* structure.

The *Mt*DXR-FMN active site contains two enclosed pockets; see Fig. 2C. The larger one, referred to earlier, is hydrated, whereas the other is smaller and bounded by the inhibitor, cofactor, and side chains of Trp-203, Met-205, and Met-267.

A comparison of *Mt*DXR-FMN with *Mt*DXR-FN and *Mt*DXR-MNS shows that they are highly similar overall. The side chains of Asp-151 and Ser-152 together with fosmidomycin show the largest changes upon metal binding (Fig. 4A), whereas the octahedral coordination around the Mn^{2+} ion seen in *Mt*DXR-MNS (Fig. 4B) is slightly distorted upon inhibitor binding in *Mt*DXR-FMN (Fig. 4A). Poor electron density is observed for residues A207 and B204–B206 in the active site flaps. In the B molecule the density for a large portion of NADPH is also very poor, and therefore, the occupancy has been set to zero except for the adenosine and its 2'-phosphate group. A Mn^{2+} ion is found in the active site of the B molecule, but only a sulfate ion is bound at the phosphonate position in the fosmidomycin binding site.

A comparison of *Mt*DXR^{NQ}-S and *Mt*DXR-S shows that Gln-222 is unchanged, whereas Asn-151 is flipped away from the metal binding site, and Glu-153 is flipped toward this area. Their active site flaps display the same conformation, although poor electron density is observed in *Mt*DXR^{NQ}-S for residues A199–A205. The structure of *Mt*DXR^{NQ}-NS shows that the mutant enzyme can bind NADPH, although the mobility of the bound cofactor is high. In the A molecule the density for the nicotinamide portion of NADPH is poor, and therefore, the occupancy has been set to zero. In the B molecule the density for NADPH is completely absent. Poor electron density is also observed for residues A185–A191, A199–A209, B205, and B387–B389. The positions of residues Asn-151, Glu-153, and Gln-222 are similar to what is observed in the *Mt*DXR^{NQ}-S structure. The *Mt*DXR^{NQ}-NS crystal was co-crystallized with $MnSO_4$, but no electron density for the metal ion can be observed.

The seventh structure, *Mt*DXR^{NQ}-FN, shows that the mutant enzyme can also bind the inhibitor fosmidomycin. The positions of residues Glu-153 and Gln-222 are similar to those observed in the *Mt*DXR^{NQ}-S and *Mt*DXR^{NQ}-NS structures, whereas residue Asn-151 is flipped even further away from the metal binding site. Poor electron density is observed for amino acids A199–A202, B199, and B204–B205. The density for NADPH is poor in both molecules, although not to the same extent as in the *Mt*DXR^{NQ}-NS structure. The occupancy for the nicotinamide ring has been set to zero in the A molecule, whereas the complete nicotinamide portion in the B molecule has been excluded from the refinement.

Comparison to Other DXR Structures—Our previous comparison (16) of 13 DXR structures from *M. tuberculosis*, *E. coli*, and *Z. mobilis* showed that the overall three-dimensional structural arrangement is conserved. However, the *Mt*DXR structure exhibits some differences from the others. These include a shorter $\alpha 3/\beta 4$ unit (residues 70–84) and shorter $\alpha 7/\beta 7$ and $\alpha 8/\beta 8$ loops (residues 142–145 and 164–169, respectively). Although the overall sequence identity is ~40%, the central catalytic domain shows a higher degree of conservation (45–50% amino acid sequence identity) than the N- and C-terminal domains (40 and 35% amino acid sequence identity, respectively). A comparison of the various DXR structures also showed that there is variation in the way that the domains move relative to each other, triggered by the binding of cofactors, substrates and inhibitors, and differences in crystal forms (21). The *E. coli* structures can be grouped into closed, open and super-open forms, as reflected in the distances across the active site cleft (Table 2). The A and B chains of *Ec*DXR (PDB code 1K5H) are the only representatives of the super-open conformation. Among the structures showing the open conformation are those binding a single substrate or inhibitor with or without a metal ion present. Structures showing closed conformations include those where both substrate and cofactor binding sites are occupied, *i.e.* *Ec*DXR-FN (with and without citric acid) and *Ec*DXR-N,DXP. *Ec*DXR-NS needs special mention since both sites are occupied but in an open conformation. Structure factors have not been deposited for this entry, and so the electron density cannot be inspected, although it is apparent that the NADPH molecules have elevated B-factors compared with the protein. This may indicate that crystal packing forces have trapped this protein conformation.

When grouping the *Mt*DXR structures by the same criteria, one can see that all B molecules as well as both A and B molecules from *Mt*DXR-S show an open conformation. The A molecules generally display a more closed conformation, although not as closed as those observed in the *E. coli* structures *Ec*DXR-FN and *Ec*DXR-N,DXP. This difference could be a consequence of the species difference. The larger variations of the distance across the active site among the *E. coli* structures may be associated with the different crystallization conditions and space groups involved. A superposition of *Mt*DXR and *Ec*DXR structures, based on their N-terminal NADPH-binding domains, is shown in Fig. 4C to illustrate the variation.

MD Simulations and Empirical Valence Bond Calculations—The free energy profiles for the proton abstraction from the O4 hydroxyl of DXP by a glutamic acid residue in solution and by Glu-153 in *Mt*DXR are shown in Fig. 5. The activation and reaction free energy in the protein are significantly lower than for the reaction in solvent; evidently the enzyme exerts a large catalytic effect on this reaction step. It is particularly noteworthy

FIGURE 4. **Changes in the structure on ligand binding.** A, stereo view of the super-positioning of the active sites of *Mt*DXR-FN (pink) and *Mt*DXR-FMN (gold), showing the movement of foremost Asp-151 and fosmidomycin in the presence or absence of Mn^{2+} . B, stereo view of the active site of *Mt*DXR-MNS showing the octahedral coordination of the Mn^{2+} ion by Asp-151, Glu-153, Glu-222, and three water molecules. C, stereo view of the structural comparisons. The *M. tuberculosis* structures *Mt*DXR-S (red), *Mt*DXR-MS (magenta), *Mt*DXR-MNS (brown), *Mt*DXR-FN (black), and *Mt*DXR-FMN (cyan) and the *E. coli* structures *Ec*DXR-N,DXP (green), *Ec*DXR (blue, PDB code 1ONN), and *Ec*DXR-FM (yellow) have been superimposed based on their N-terminal domains (α atoms) with the *lsq-explicit* command in O (32). The *M. tuberculosis* enzyme displays a smaller movement of the domains than the *E. coli* enzyme upon the binding of different substrates and cofactors. D, stereo view of the active site of *Mt*DXR-FMN with models of DXP (magenta) and MEP (cyan) super-positioned onto our experimentally observed fosmidomycin structure. Golden bubbles show the observed interactions with the Mn^{2+} ion. Magenta and cyan bubbles indicate the close contacts between the ion and the O4 and O3 hydroxyl groups of DXP and MEP, respectively.

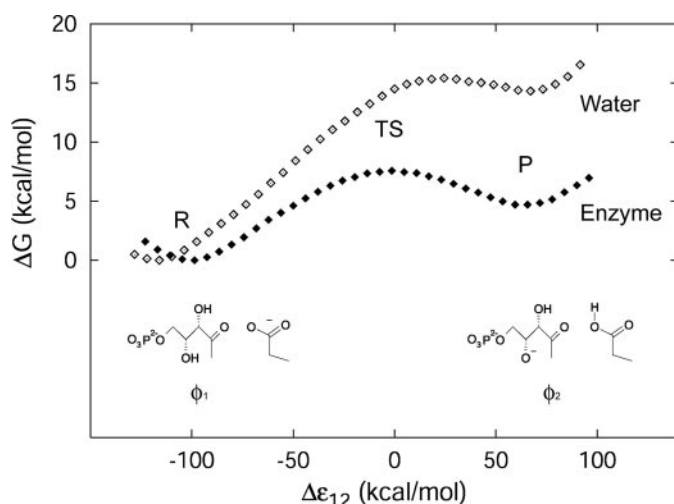


FIGURE 5. **Reaction free energy profiles.** Calculated free energy profiles for the proton abstraction from the O4 hydroxyl by a glutamic acid in solution (open diamonds) and by Glu-153 in *Mt*DXR (filled diamonds). The reaction coordinate, $\Delta\epsilon_{12}$, is the energy difference between the two valence bond states ϕ_1 and ϕ_2 . The reactants (R) and products (P) corresponding to ϕ_1 and ϕ_2 , respectively, are shown below the free energy profiles. In the enzyme the transition state (TS) is stabilized by more than 7 kcal/mol compared with the corresponding uncatalyzed reaction in solution.

thy that the effective pK_a difference between the donor and acceptor is reduced by about 7 pK units (equivalent to 10 kcal/mol) making the predicted initial reaction step almost isoergonic.

DISCUSSION

The sequence corresponding to *M. tuberculosis* Rv2870c codes for a fully functional DXR (16, 49, 50). Our previous construct, which contained a C-terminal truncation of 20 amino acids, showed similar kinetic parameters to the full-length and a proteolytically cleaved enzyme (49) truncated by 18 amino acids. The even shorter construct used here showed similar activity, indicating that a C-terminal truncation of 24 amino acids still results in an active enzyme. We have now also shown that the inhibitor fosmidomycin, at an enzyme concentration of 0.35 μ M and substrate concentrations of 0.2 mM DXP and 0.1 mM NADPH, inhibits the enzyme with an estimated IC_{50} value of 80 nM. This is similar to values of 310 and 30 nM that have been published for the *M. tuberculosis* and *E. coli* enzymes, respectively (50, 51). A double mutant of *Mt*DXR, containing the substitutions D151N and E222Q (*Mt*DXR^{NQ}), represents a completely inactive enzyme, emphasizing the importance of these residues in metal binding and catalysis. Mn^{2+} was used in all activity measurements and most of the crystallization experiments. Where added, it was clearly observed in all electron density maps, except for the *Mt*DXR^{NQ}-NS structure.

Crystallography is usually considered to provide a static view of an enzyme structure. However, by solving structures of different crystal forms with and without different substrates, inhibitors, ligands, and cofactors, one can build up insights into the dynamic properties of an enzyme. Extensive studies on the *Ec*DXR (listed in Table 2) indicate well defined catalytic domains that provide much of the rather rigid dimer interface. The N-terminal NADPH binding and C-terminal domains

move as rigid bodies with respect to the catalytic domain under the influence of ligand/substrate binding and crystal contacts. Our structural studies of *Mt*DXR show similar effects. In the structures presented here, crystal contacts stabilize an open active site in the B molecule. The active site in the A molecule is more closed, although some variation is possible depending on the binding of ligands and substrates. An active site flap is present in both *E. coli* and *M. tuberculosis* enzymes. Well defined density for the *M. tuberculosis* flap requires well defined density for the complete NADPH cofactor in the closed active site cleft. It may be of particular relevance that in the best-defined structures, the main-chain nitrogen of Gly-206 interacts with the nicotinamide phosphate, and the side chain of Asn-209 interacts with the nicotinamide sugar and ring. The side chains of two flap residues, Trp-203 and Met-205, help to shield the substrate, whereas a third, His-200, contributes to the binding of the substrate phosphate group. All five residues are highly conserved among DXR enzymes (47).

The structures reveal that the mutant can still bind NADPH, sulfate, and fosmidomycin but that it has lost its ability to bind the metal ion, which in turn causes loss of activity. In the *Mt*DXR structure with a sulfate in the active site (PDB code 2C82) (16) the short distance of 2.45 Å between Asp-151 (OD1) and Glu-222 (OE2) suggests that one of these residues has to be protonated, which is unsurprising given the pH of ~5.1 used to produce crystals. In *Mt*DXR^{NQ}-S the interaction is lost, which seems to affect not only the metal binding but also NADPH binding. By comparing the mutant structures with the corresponding wild type structures, for example *Mt*DXR^{NQ}-FN and *Mt*DXR-FN, one can see that the position of NADPH is less defined in the mutant. The collection of structures also shows that the adenosine part of NADPH and especially the 2'-phosphate bound to it is better defined than the nicotinamide part, confirming the importance of this group for binding, as previously proposed (49).

By comparing the structures of *Mt*DXR-FN and *Mt*DXR-FMN, it can be seen that the metal binding residues and the (*N*-formyl-*N*-hydroxy) amino group of the inhibitor must move to coordinate the metal. By contrast, the positions of the phosphonate part of the inhibitor and of NADPH remain fixed. Comparison of *Mt*DXR-FN with *Ec*DXR-FN shows that the position of the inhibitors in these structures is equivalent. However, when comparing *Mt*DXR-FMN and the *E. coli* structure in complex with fosmidomycin and Mn^{2+} (PDB code 1ONP) (19) it becomes clear that the conformation of the inhibitor is different. This could be due to the lack of NADPH in the 1ONP structure, *i.e.* a real effect, or to a misinterpretation of the crystallographic results. The 1ONP study was carried out at 2.5 Å resolution and clearly showed that the inhibitor was bound in the active site. However, since structure factor data are not available, we are unable to evaluate which mode of ligand (and possibly water) binding is in best agreement with their experimental data. The coordination around the metal ion has important mechanistic consequences. The production of MEP from DXP is carried out in two steps, an isomerization followed by an NADPH-dependent reduction. The intramolecular rearrangement of DXP to form the aldehyde intermediate, 2-C-methylerythrose 4-phosphate, is thought to occur via a retroaldoliza-

tion or an α -ketol rearrangement (52). Three different studies of DXRs from the cyanobacterium *Synechocystis* (53), *E. coli* (54), and *M. tuberculosis* (49) agree that the *pro*-R hydrogen of C1 of MEP is derived from the 4S-H of NADPH in the reduction step. However, the mode of fosmidomycin binding reported in the 1ONP structure is not suitable for this stereochemistry. To explain the stereochemistry of the hydride transfer from this model, a rearrangement of the intermediate 2-C-methylerythrose 4-phosphate around the Mn^{2+} ion was, therefore, proposed (19). This new coordination would in fact be directly equivalent to a fosmidomycin binding mode that we observe in our structure. In Figs. 3B and 4D we have made a simple modeling experiment of the substrate and product binding based on the position of fosmidomycin observed in our *Mt*DXR-FMN structure. In this model, hydride transfer from C4 of NADPH can take place to provide the stereochemically correct product and without major rearrangement of the metal coordination. Furthermore, in *Mt*DXR-FMN, the hydrogen atom of NADPH is transferred from the position below C4 in the nicotinamide ring, which would be appropriate if DXR is a class B dehydrogenase, as proposed earlier (21) and as suggested by the stereochemical course of the reaction (49, 53, 54). Our model for substrate binding may provide yet another mechanistic insight. The O4 hydroxyl of our DXP model comes close to the unoccupied Mn^{2+} coordination site and to the carboxylate group of Glu-153 (Fig. 4D). Glu-153 is, therefore, ideally positioned for the proton abstraction step, which leads to the known enzyme intermediate via a proposed retroaldolization mechanism (52). We have evaluated the likelihood of this proton transfer step using MD simulations and free energy calculations. The free energy profiles, which showed that the enzyme exerts a large catalytic effect on the reaction, therefore provide support for the first step in a possible retroaldolization mechanism. Both of the isomerization mechanisms (52) also require at some stage deprotonation of the DXP O3 hydroxyl group, and Glu-222 is suitably positioned for such a task.

Our main interest in studying *Mt*DXR is to contribute toward the development of new drugs against *M. tuberculosis*. Fosmidomycin is not active against *M. tuberculosis* (50), although it is active against *Plasmodium* species that cause malaria (13–15). It has been suggested that the only possibilities to build upon the fosmidomycin scaffold would require either a displacement of the nicotinamide ring of NADPH or targeting the open conformation of DXR (21). Our studies suggest otherwise. Fosmidomycin-like compounds have already been produced that are more active than fosmidomycin against *P. falciparum* (51). We believe that the most active of these new compounds (with a 3,4-dichlorophenyl substitution at the C4 atom of fosmidomycin) does not extend into the NADPH site but that instead it extends into the hydrated cavity, lined by highly conserved amino acids (Thr-175, Ser-245, and His-248) (47), that is located close to the substrate binding site. As far as we know this compound has not been tested on mycobacteria, although, as for fosmidomycin itself, the phosphonate group makes it unlikely that the compound will be transported into *M. tuberculosis*. Although efforts should be made to replace the phosphonate group with one that is more compatible with bacterial uptake, this does not preclude the use of the NADPH

binding site as a target for the design of new inhibitors. Initial attempts at targeting the NADPH binding site have already produced mimics that bind with ~ 200 nM affinity (55), which provides incentive for further efforts. No compounds have yet been produced, however, that make full use of the binding potential available in the active site of DXR. Our structural work, therefore, provides a strong framework for the design of DXR inhibitors, with the desired bacteriocidal activities.

Acknowledgments—We are grateful to AstraZeneca India Pvt. Ltd for providing the template plasmid, the inhibitor fosmidomycin, and the substrate 1-deoxy-D-xylulose 5-phosphate. We are also thankful to Evalena Andersson, Annette Roos, Johan Unge, Alina Castell, Patrik Johansson, Anna Jansson, and Emma Jakobsson for assistance in data collection.

REFERENCES

1. Rohmer, M. (1999) *Nat. Prod. Rep.* **16**, 565–574
2. Rohmer, M., Knani, M., Simonin, P., Sutter, B., and Sahm, H. (1993) *Biochem. J.* **295**, 517–524
3. Lichtenthaler, H. K. (1999) *Annu. Rev. Plant Physiol. Plant Mol. Biol.* **50**, 47–65
4. Sacchettini, J. C., and Poulter, C. D. (1997) *Science* **277**, 1788–1789
5. Boucher, Y., and Doolittle, W. F. (2000) *Mol. Microbiol.* **37**, 703–716
6. Spurgeon, S. L., and Porter, J. W. (1981) in *Biosynthesis of isoprenoid Compounds* (Porter, J. W., and Spurgeon, S. L.) pp. 1–46, John Wiley & Sons, Inc., New York
7. Takahashi, S., Kuzuyama, T., Watanabe, H., and Seto, H. (1998) *Proc. Natl. Acad. Sci. U. S. A.* **95**, 9879–9884
8. Kobayashi, K., Ehrlich, S. D., Albertini, A., Amati, G., Andersen, K. K., Arnaud, M., Asai, K., Ashikaga, S., Aymerich, S., Bessieres, P., Boland, F., Brignell, S. C., Bron, S., Bunai, K., Chapuis, J., Christiansen, L. C., Danchin, A., Debarbouille, M., Dervyn, E., Deuerling, E., Devine, K., Devine, S. K., Dreesen, O., Errington, J., Fillinger, S., Foster, S. J., Fujita, Y., Galizzi, A., Gardan, R., Eschevins, C., Fukushima, T., Haga, K., Harwood, C. R., Hecker, M., Hosoya, D., Hulio, M. F., Kakeshita, H., Karamata, D., Kasa-hara, Y., Kawamura, F., Koga, K., Koski, P., Kuwana, R., Imamura, D., Ishimaru, M., Ishikawa, S., Ishio, I., Le Coq, D., Masson, A., Mauel, C., Meima, R., Mellado, R. P., Moir, A., Moriya, S., Nagakawa, E., Nanamiya, H., Nakai, S., Nygaard, P., Ogura, M., Ohanan, T., O'Reilly, M., O'Rourke, M., Pragai, Z., Pooley, H. M., Rapoport, G., Rawlins, J. P., Rivas, L. A., Rivolta, C., Sadaie, A., Sadaie, Y., Sarvas, M., Sato, T., Saxild, H. H., Scanlan, E., Schumann, W., Seegers, J. F., Sekiguchi, J., Sekowska, A., Seror, S. J., Simon, M., Stragier, P., Studer, R., Takamatsu, H., Tanaka, T., Takeuchi, M., Thomaidis, H. B., Vagner, V., van Dijk, J. M., Watabe, K., Wipat, A., Yamamoto, H., Yamamoto, M., Yamamoto, Y., Yamane, K., Yata, K., Yoshida, K., Yoshikawa, H., Zuber, U., and Ogasawara, N. (2003) *Proc. Natl. Acad. Sci. U. S. A.* **100**, 4678–4683
9. Rodriguez-Concepcion, M., Campos, N., Maria Lois, L., Maldonado, C., Hoeffler, J. F., Grosdemange-Billiard, C., Rohmer, M., and Boronat, A. (2000) *FEBS Lett.* **473**, 328–332
10. Shigi, Y. (1989) *J. Antimicrob. Chemother.* **24**, 131–145
11. Kuzuyama, T., Shimizu, T., Takahashi, S., and Seto, H. (1998) *Tetrahedron Lett.* **39**, 7913–7916
12. Zeidler, J., Schwender, J., Muller, C., Wiesner, J., Weidemeyer, C., Beck, E., Jomaa, H., and Lichtenthaler, H. K. (1998) *Z. Naturforsch. C* **53**, 980–986
13. Missinou, M. A., Borrmann, S., Schindler, A., Issifou, S., Adegnik, A. A., Matsiegui, P. B., Binder, R., Lell, B., Wiesner, J., Baranek, T., Jomaa, H., and Kremsner, P. G. (2002) *Lancet* **360**, 1941–1942
14. Lell, B., Ruangweera, R., Wiesner, J., Missinou, M. A., Schindler, A., Baranek, T., Hintz, M., Hutchinson, D., Jomaa, H., and Kremsner, P. G. (2003) *Antimicrob. Agents Chemother.* **47**, 735–738
15. Jomaa, H., Wiesner, J., Sanderbrand, S., Altincicek, B., Weidemeyer, C., Hintz, M., Turbachova, I., Eberl, M., Zeidler, J., Lichtenthaler, H. K., Sol-

- dati, D., and Beck, E. (1999) *Science* **285**, 1573–1576
16. Henriksson, L. M., Björkelid, C., Mowbray, S. L., and Unge, T. (2006) *Acta Crystallogr. Sect. D Biol. Crystallogr.* **62**, 807–813
17. Berman, H. M., Westbrook, J., Feng, Z., Gilliland, G., Bhat, T. N., Weissig, H., Shindyalov, I. N., and Bourne, P. E. (2000) *Nucleic Acids Res.* **28**, 235–242
18. Reuter, K., Sanderbrand, S., Jomaa, H., Wiesner, J., Steinbrecher, I., Beck, E., Hintz, M., Klebe, G., and Stubbs, M. T. (2002) *J. Biol. Chem.* **277**, 5378–5384
19. Steinbacher, S., Kaiser, J., Eisenreich, W., Huber, R., Bacher, A., and Rohdich, F. (2003) *J. Biol. Chem.* **278**, 18401–18407
20. Yajima, S., Nonaka, T., Kuzuyama, T., Seto, H., and Ohsawa, K. (2002) *J. Biochem. (Tokyo)* **131**, 313–317
21. MacSweeney, A., Lange, R., Fernandes, R. P., Schulz, H., Dale, G. E., Douangamath, A., Proteau, P. J., and Oefner, C. (2005) *J. Mol. Biol.* **345**, 115–127
22. Yajima, S., Hara, K., Sanders, J. M., Yin, F., Ohsawa, K., Wiesner, J., Jomaa, H., and Oldfield, E. (2004) *J. Am. Chem. Soc.* **126**, 10824–10825
23. Ricagno, S., Grolle, S., Bringer-Meyer, S., Sahm, H., Lindqvist, Y., and Schneider, G. (2004) *Biochim. Biophys. Acta* **1698**, 37–44
24. Cole, S. T., Brosch, R., Parkhill, J., Garnier, T., Churcher, C., Harris, D., Gordon, S. V., Eiglmeier, K., Gas, S., Barry, C. E., 3rd, Tekaia, F., Badcock, K., Basham, D., Brown, D., Chillingworth, T., Connor, R., Davies, R., Devlin, K., Feltwell, T., Gentles, S., Hamlin, N., Holroyd, S., Hornsby, T., Jagels, K., and Barrell, B. G. (1998) *Nature* **393**, 537–544
25. Kuzuyama, T., Takahashi, S., Watanabe, H., and Seto, H. (1998) *Tetrahedron Lett.* **39**, 4509–4512
26. Leslie, A. G. (1999) *Acta Crystallogr. Sect. D* **55**, 1696–1702
27. Evans, P. R. (1993) in *Proceedings of CCP4 Study Weekend on Data Collection and Processing* (Sawyer, L., Isaac, N., and Bailey, S., eds) pp. 114–122, Daresbury Laboratory, Warrington, England
28. Collaborative Computing Project 4 (1994) *Acta Crystallogr. Sect. D* **50**, 760–763
29. Matthews, B. W. (1968) *J. Mol. Biol.* **33**, 491–497
30. Navaza, J. (1994) *Acta Crystallogr. Sect. A* **50**, 157–163
31. Murshudov, G., Vagin, A., and Dodson, E. (1997) *Acta Crystallogr. Sect. D* **53**, 240–255
32. Jones, T. A., Zou, J. Y., Cowan, S. W., and Kjeldgaard (1991) *Acta Crystallogr. Sect. A* **47**, 110–119
33. Lamzin, V. S., and Wilson, K. S. (1993) *Acta Crystallogr. Sect. D* **49**, 129–147
34. Harris, M., and Jones, T. A. (2001) *Acta Crystallogr. Sect. D* **57**, 1201–1203
35. Åqvist, J., and Warshel, A. (1993) *Chem. Rev.* **93**, 2523–2544
36. Warshel, A. (1991) *Computer Modeling of Chemical Reactions in Enzymes and Solutions*, John Wiley & Sons, Inc., New York
37. Bayly, C. I., Cieplak, P., Cornell, W. D., and Kollman, P. A. (1993) *J. Phys. Chem.* **97**, 10269–10280
38. MacKerell, A. D., Wiorkiewicz-Kuczera, J., and Karplus, M. (1995) *J. Am. Chem. Soc.* **117**, 11946–11975
39. Eigen, M. (1964) *Angew. Chem. Int. Ed. Engl.* **3**, 1–72
40. Åqvist, J. (1997) in *Computational Approaches to Biochemical Reactivity* (Náray-Szabó, G., and Warshel, A.) pp. 341–362, Kluwer Academic Publishers
41. Jones, G., Willett, P., Glen, R. C., Leach, A. R., and Taylor, R. (1997) *J. Mol. Biol.* **267**, 727–748
42. Jorgensen, W. L., Chandrasekhar, J., Madura, J. D., Impey, R. W., and Klein, M. L. (1983) *J. Chem. Phys.* **79**, 926–935
43. Marelus, J., Kolmodin, K., Feierberg, I., and Åqvist, J. (1998) *J. Mol. Graph. Model.* **16**, 213–225
44. Cornell, W. D., Cieplak, P., Bayly, C. I., Gould, I. R., Merz, K. M., Ferguson, D. M., Spellmeyer, D. C., Fox, T., Caldwell, J. W., and Kollman, P. A. (1995) *J. Am. Chem. Soc.* **117**, 5179–5197
45. Holmberg, N., Ryde, U., and Bulow, L. (1999) *Protein Eng.* **12**, 851–856
46. Bjelic, S., and Åqvist, J. (2006) *Biochemistry* **45**, 7709–7723
47. Kuzuyama, T., Takahashi, S., Takagi, M., and Seto, H. (2000) *J. Biol. Chem.* **275**, 19928–19932
48. Levitt, M., and Perutz, M. F. (1988) *J. Mol. Biol.* **201**, 751–754
49. Argyrou, A., and Blanchard, J. S. (2004) *Biochemistry* **43**, 4375–4384
50. Dhiman, R. K., Schaeffer, M. L., Bailey, A. M., Testa, C. A., Scherman, H., and Crick, D. C. (2005) *J. Bacteriol.* **187**, 8395–8402
51. Haemers, T., Wiesner, J., Van Poecke, S., Goeman, J., Henschker, D., Beck, E., Jomaa, H., and Van Calenbergh, S. (2006) *Bioorg. Med. Chem. Lett.* **16**, 1888–1891
52. Hoeffler, J. F., Tritsch, D., Grosdemange-Billiard, C., and Rohmer, M. (2002) *Eur. J. Biochem.* **269**, 4446–4457
53. Proteau, P. J., Woo, Y. H., Williamson, R. T., and Phaosiri, C. (1999) *Org. Lett.* **1**, 921–923
54. Radykewicz, T., Rohdich, F., Wungsintaweekul, J., Herz, S., Kis, K., Eisenreich, W., Bacher, A., Zenk, M. H., and Arigoni, D. (2000) *FEBS Lett.* **465**, 157–160
55. Sem, D. S., Bertolaet, B., Baker, B., Chang, E., Costache, A. D., Coutts, S., Dong, Q., Hansen, M., Hong, V., Huang, X., Jack, R. M., Kho, R., Lang, H., Ma, C. T., Meininger, D., Pellicchia, M., Pierre, F., Villar, H., and Yu, L. (2004) *Chem. Biol.* **11**, 185–194
56. Read, R. J. (1986) *Acta Crystallogr. Sect. A* **42**, 140–149
57. Diederichs, K., and Karplus, P. A. (1997) *Nat. Struct. Biol.* **4**, 269–275
58. Kleywegt, G. J., and Jones, T. A. (1996) *Structure* **4**, 1395–1400
59. Engh, R., and Huber, R. (1991) *Acta Crystallogr. Sect. A* **47**, 392–400